18.73% Efficient and Stable Inverted Organic Photovoltaics Featuring a Hybrid Hole-Extraction Layer

Yuanbao Lin^{a,b}*, Yadong Zhang^c, Artiom Magomedov^d, Eleftheria Gkogkosi^e, Junxiang Zhang^c, Xiaopeng Zheng^a, Abdulrahman El-Labban^a, Stephen Barlow^c, Vytautas Getautis^d, Ergang Wang^h, Leonidas Tsetseris^e, Seth R Marder^d, Iain McCulloch^b, Thomas D. Anthopoulos^a*

Corresponding Authors

*Email: thomas.anthopoulos@kaust.edu.sa

*Email: yuanbao.lin@chem.ox.ac.uk

^a King Abdullah University of Science and Technology (KAUST), KAUST Solar Center (KSC) Thuwal 23955, Saudi Arabia

^b Department of Chemistry, University of Oxford, Oxford, OX1 3TA, UK

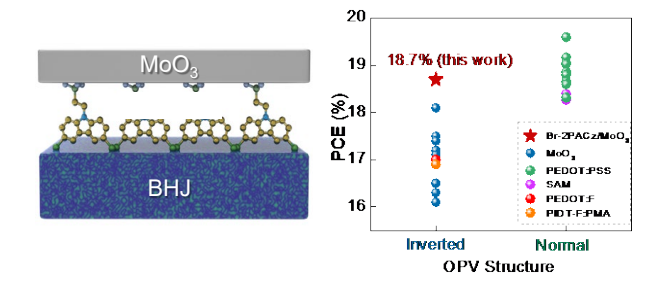
^c Renewable and Sustainable Energy Institute, Department of Chemistry, and Department of Chemical and Biological Engineering, University of Colorado Boulder, Boulder, CO 80303, USA

^d Department of Organic Chemistry, Kaunas University of Technology, Kaunas LT-50254, Lithuania

^e Department of Physics, School of Applied Mathematical and Physical Sciences, National Technical University of Atheeqens, Athens GR-15780, Greece

^h Department of Chemistry and Chemical Engineering, Chalmers University of Technology, Göteborg, SE-412 96, Sweden

TOC GRAPHICS



ABSTRACT

Developing efficient and stable organic photovoltaics (OPVs) is crucial for the technology's commercial success. However, combining these key attributes remains challenging. Herein we incorporate the small molecule 2-(3,6-dibromo-9H-carbazol-9-yl)ethyl)phosphonic acid (Br-2PACz) between the bulk-heterojunction (BHJ) and a 7-nm-thin layer of MoO₃ in inverted OPVs, and study its effects on the cell performance. We find the Br-2PACz/MoO₃ hole-extraction layer (HEL) boosts the cell's power conversion efficiency (PCE) from 17.36% to 18.73% (uncertified), making them the most efficient inverted OPVs to date. The factors responsible for this improvement include enhanced charge transport, reduced carrier recombination, and favourable vertical phase separation of donor and acceptor components in the BHJ. The Br-2PACz/MoO₃based OPVs exhibit higher operational stability under continuous illumination and thermal annealing (80 °C). The T₈₀ lifetime of OPVs featuring Br-2PACz/MoO₃ -taken as the time over which the cell's PCE reduces to 80% of its initial value—increases compared to MoO₃-only cells from 297 to 615 h upon illumination and from 731 to an astonishing 1064 h upon continuous heating. Elemental analysis of the BHJs reveals the enhanced stability to originate from the partially suppressed diffusion of Mo ions into BHJ and the favourable distribution of the donor and acceptor components induced by the Br-2PACz.

Main Text

Organic photovoltaics (OPVs) is an emerging solar-cell technology that offers various attractive attributes, including inexpensive and scalable fabrication, mechanically flexible, and environmental friendliness. ¹⁻⁹ To date, the reported power conversion efficiencies (PCEs) of single-junction OPVs have already reached 19% ¹⁰⁻¹³ and are fast approaching the maximum theoretical PCE (>20%) for single-junction OPVs. ¹⁴ The rapid increase in the efficiencies of OPVs witnessed in recent years can be attributed primarily to the development of new generations of high-performance photoactive materials and molecular dopants ^{15, 16}, as well as to significant advances in formulation engineering of the organic bulk-heterojunction (BHJ). ¹⁷⁻¹⁹

The recent progress towards high-efficiency OPVs has also prompted further commercialization efforts. However, the limited operational stability of state-of-the-art OPVs remains a formidable scientific and technological challenge. OPVs featuring inverted cell architectures are often used to reduce the degradation by exploring different metal oxides as the hole-transporting (HTL)/hole-extraction layer (HEL) and electron-transporting layer (ETL). Since most levant metal oxides exhibit outstanding stability, the corresponding inverted architecture has become a popular choice in commercial products. He highest PCEs reported thus far for OPVs with both inverted and conventional (also known as standard) architectures are summarised in **Table S1**. Although inverted OPVs are known for their longer operational lifetimes, he is their PCEs operational lifetimes, he is the process of the pr

Recently, self-assembled monolayers (SAMs) of [2-(9*H*-carbazol-9-yl)ethyl]phosphonic acid (2PACz) and its derivatives were used as nm-thin HELs on ITO for OPVs.³⁸⁻⁴³The resulting cells exhibited higher PCEs and better operational lifetime than control OPVs made with the commercial hole-conducting polymer poly(3,4-ethylenedioxythiophene) polystyrene sulfonate (PEDOT:PSS). Although the operational lifetime of SAM-based OPVs was longer than control cells with PEDOT:PSS, their operational stability remains inferior to that achieved in state-of-the-art inverted OPVs. Unfortunately, the HEL in the vast majority of inverted OPVs is molybdenum trioxide (MoO₃) (**Table S1**), which is known to diffuse into BHJ and degrade the cell performance during aging tests.⁴⁴ Thus, the development of alternative HEL materials has been receiving increasing attention in recent years primarily due to their potential for application in commercially-relevant inverted OPV architectures.

In our effort to address this timely goal, we developed a hybrid HEL composed of the (2-(3,6-dibromo-9*H*-carbazol-9-yl)ethyl)phosphonic acid) (Br-2PACz)^{38, 42} and MoO₃ (Br-2PACz/MoO₃). The performance characteristics of best-in-class OPVs featuring the hybrid HEL were then compared against cells featuring the same BHJ but using MoO₃ as the HEL. Impressively, use of the hybrid Br-2PACz/MoO₃ HEL leads to a significantly enhanced PCE and stability upon continuous illumination (100 mW/cm²) and thermal stressing (80 °C). With the help of complementary characterization techniques, we unravelled the multiple roles of Br-2PACz in increasing the PCE and stability of the ensuing inverted OPVs. Firstly, the lower surface energy of Br-2PACz/MoO₃ (43.7 mN/m), compared to MoO₃ (59.7 mN/m), is similar to the ETL's (42.8 mN/m) and defines the vertical stratification of the BHJ components. Secondly, the higher work function of the hybrid Br-2PACz/MoO₃ HEL improves hole extraction and, ultimately, the overall performance of the resulting OPVs. These additional functionalities boost the PCE of the

corresponding OPVs from 17.36% (MoO₃) to 18.73% (Br-2PACz/MoO₃) (uncertified). Critically, we find Br-2PACz/MoO₃ HEL prolongs the cell's operational lifetime by partially suppressing the diffusion of Mo ions from MoO₃ into the BHJ while simultaneously inhibiting the vertical phase separation of the donor(s) and the acceptor components. Consequently, the T₈₀ lifetime of the cells -defined as the time taken for PCE to drop to 80% of its initial value- increased from 297 to 615 h under continuous illumination and from 731 to a whopping 1064 h upon continuous heating when MoO₃ is replaced with the hybrid Br-2PACz/MoO₃ HEL.

Fig. 1a shows the inverted OPV architecture developed consisting of ITO/ZnO/PEN-Br/BHJ/Br-2PACz/MoO₃/Ag, where ZnO/PFN-Br is a known bilayer ETL⁴⁵ and PM6:PM7-Si:BTP-eC9 is the ternary BHJ blend used throughout this study (Fig. S1)^{42, 46}. To form the hybrid HEL, Br-2PACz was first spin-coated onto the BHJ, followed by the processing of a 7-nm-thin MoO₃ layer via thermal vacuum sublimation (see **Supporting Information**). We chose Br-2PACz because of its recently demonstrated superior HEL functionality in high-performance OPVs based on the standard architecture.^{38, 42} The Br-2PACz coverage over the BHJ layer was assessed by energy-dispersive X-ray spectroscopy (EDX) mapping using a scanning electron microscope (SEM). The presence of Br-2PACz was probed by measuring the Br content via EDX (Fig. S2). The results confirm the uniform coverage of the BHJ's surface by the Br-2PACz layer. Atomic force microscopy (AFM) measurements were also performed to visualize the surface topographies of the PM6:PM7-Si:BTP-eC9 BHJ before and after Br-2PACz deposition (Fig. S3). The ternary BHJ exhibits a well-defined fibril network surface topography, previously linked to improved exciton dissociation and charge transport in OPVs. 40 The Br-2PACz appears to form an ultra-thin layer atop the BHJ. No topographical differences can be discerned between the surface of the BHJ and the BHJ/Br-2PACz, although the root mean square (RMS) value of the surface roughness of BHJ/Br-2PACz is slightly lower (0.99 nm) than that of the pristine BHJ (1.16 nm). This characteristic smoothing effect is better illustrated in the surface height histograms of **Fig. S3e**, where the peak of the distribution for the BHJ/Br-2PACz undergoes a clear shift towards zero. This is an important finding since the existence of a smoother interface was previously associated with a lower contact resistance in pertinent devices⁴⁷ and, as such, is expected to play a positive role in charge extraction. From the data presented thus far, we conclude that solution processing of Br-2PACz directly onto the BHJ forms a continuous and conformal layer a few nanometers in thickness. In addition, the BHJ after spin-coating with pure ethanol exhibits a similar RMS value (1.40 nm *vs.* 1.38 nm) and a surface height histogram as compared to pristine BHJ according to AFM in **Fig. S3**, suggesting that pure ethanol solvent impacts negligibly in the surface morphology of BHJ.

To gain further insights into the electrical properties of devices, we performed electrochemical impedance spectroscopy (EIS) measurements on complete cells featuring MoO₃ and Br-2PACz/MoO₃ as the HEL. **Fig. S4a** shows the Nyquist plots measured for the different cells, while **Table S2** summarises the fitting parameters to the equivalent circuit model used (**Fig. S4b**). OPVs with Br-2PACz/MoO₃ exhibit lower interface resistance (R_{int}) than devices with MoO₃ but with comparable electrode resistance (R_{ele}). The lower R_{int} in devices (**Table S2**) with Br-2PACz/MoO₃ is attributed to the smoothing effect the Br-2PACz has on the BHJ surface, resulting in a more planarized contact with MoO₃ as suggested by the AFM analysis in **Fig. S3g**. We also note that the BHJ resistance (R_{bhj}) in devices featuring Br-2PACz/MoO₃ HEL is lower compared to cells based on MoO₃. This finding indicates significant electronic differences between the two interfaces, which may stem from changes in the composition of the BHJ close to the interface with the corresponding electrode.

The surface energies (γ) of the donor, acceptor, and interlayer materials were measured using the Owens method (**Fig. S5** and **Table S3**) in order to identify the existence of forces that could drive compositional changes in the BHJ closer to the interface. The non-fullerene acceptor (NFA) BTP-eC9 yielded a γ value of 29.5 mN/m, which is higher than the two polymer donors PM6 (20.3 mN/m) and PM7-Si (22.3 mN/m). In the case of the interlayers, the pristine MoO₃ showed a much higher γ value than the ZnO/PFN-Br ETL (59.7 vs 42.8 mN/m). However, its surface energy reduces from 59.7 to 43.7 mN/m upon Br-2PACz functionalization. Differences in γ values for the various materials have been previously shown to affect the vertical stratification of the donor and acceptor components across the BHJ and ultimately the cell's overall performance.⁴⁹

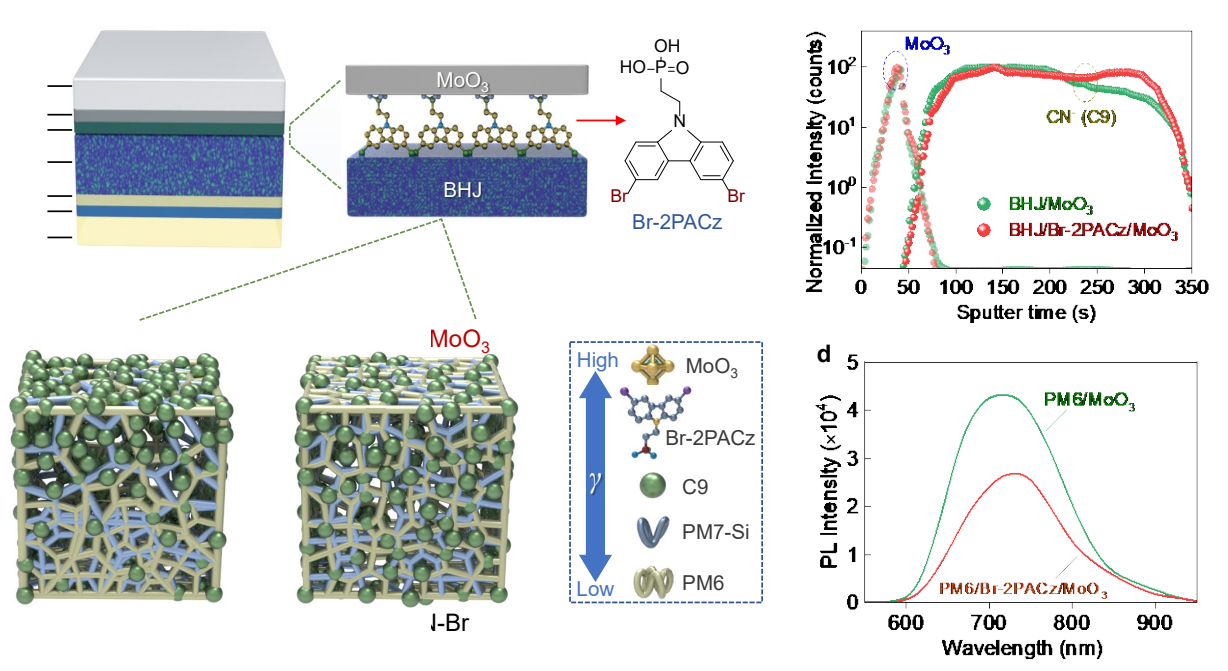


Fig. 1. (a) The schematic architecture of the OPVs used. The zoom-in shows the location of the Br-2PACz layer between the BHJ and MoO₃. (b) The ToF-SIMS intensity against the sputtering time in the MoO₃-only and the Br-2PACz/MoO₃ BHJ devices. (c) Schematics depict the BHJ components' distribution in MoO₃ and Br-2PACz/MoO₃-based OPVs. The blue arrow indicates the trend in the surface energy (γ), from high to low, of the various materials used to construct the cells. (d) The PL spectra of PM6 spin-coated films onto evaporated MoO₃ layer and MoO₃ functionalized with Br-2PACz (Br-2PACz/MoO₃) under 400 nm excitation.

To directly probe the vertical stratification of the donor and the acceptor moieties in MoO₃only and Br-2PACz/MoO₃-based cells, we used time-of-flight secondary ion mass spectrometry (ToF-SIMS). As shown in Fig. 1b, in the case of a MoO₃, the CN⁻ signal associated with the BTPeC9 weakens gradually with the increased sputtering time (depth), implying that BTP-eC9 molecules accumulate closer to the BHJ/MoO₃ interface. Concomitantly, the two donor polymers, PM6 and PM7, appear to aggregate closer to the ETL (i.e. ZnO/PFN-Br) interface (Fig. S6). The decreased/increased signals associated with the acceptor/donor components vs sputtering time are suppressed in devices featuring the hybrid Br-2PACz/MoO₃ HEL, showing more constant intensities across the BHJ. The latter feature indicates a more uniform component distribution and highlights the critical role of the top HEL in driving the phase separation between the donor/acceptor materials. Fig. 1c schematically depicts the distribution of the donor and acceptor in devices with MoO₃ and Br-2PACz/MoO₃ HEL, as suggested by the ToF-SIMS results. In the former, the NFA segregates closer to the BHJ/HEL interface, while the concentration of the donor polymer appears higher at the BHJ/ETL interface (Fig. 1b). In the case of Br-2PACz/MoO₃, both the donor and acceptors are more uniformly distributed across the BHJ. The vertical stratification of donor and acceptor plays a vital role in charge transport and carrier recombination in OPV devices. ^{50, 51} Supporting evidence comes from the photoluminescence (PL) quenching experiments performed in PM6/MoO₃ and PM6/Br-2PACz/MoO₃ samples (Fig. 1d). The more substantial PL quenching was observed in the latter sample, which is consistent with increased exciton dissociation, most likely due to the formation of a more optimal PM6/HEL heterointerface. Furthermore, because of the poor solubility of PM6 and BTP-eC9 in ethanol (Fig. S7a), the CN⁻ signal in BHJ after spin-coated with pure ethanol solvent (Fig. S7b), is similar to that without solvent treatment, suggesting that the ethanol solvent make a negligible effect in the vertical stratification of BHJ.

Next, ultraviolet photoelectron spectroscopy (UPS) was used to determine the WF of the various HELs. To emulate the structure of the hole-collecting electrode used in the actual OPVs, a silver (Ag) electrode was deposited first onto a glass substrate, followed by the MoO₃ deposition to form the Ag/MoO₃. The Ag/MoO₃/Br-2PACz structure was then formed by spin-coating the Br-2PACz onto the Ag/MoO₃ electrode (see *Supporting Information*). From the data shown in **Fig. S8**, we obtain WF values of 5.32 and 5.58 eV for the Ag/MoO₃ and Ag/MoO₃/Br-2PACz, respectively. The UPS data are corroborated by the Kelvin Probe (KP) measurements summarised in **Table S4**, further verifying the crucial role of the Br-2PACz in increasing the WF of the hybrid HEL. The larger WF is anticipated to improve the hole extraction from the BHJ and increase the cell's PCE. ^{52, 53}

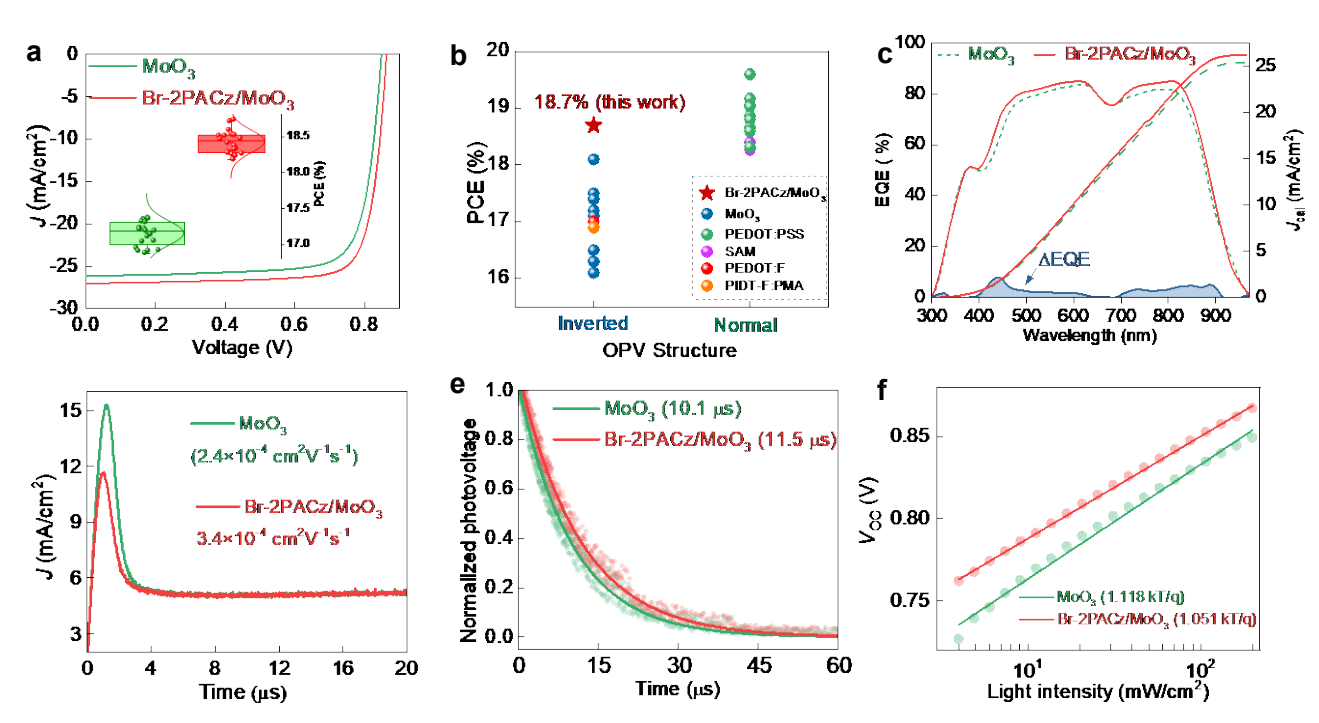


Fig. 2. (a) *J-V* curves for OPVs employing MoO₃ and Br-2PACz/MoO₃ as the hole-extracting layers. The inset shows box charts of PCEs for twenty cells per batch made using MoO₃ (green)

and Br-2PACz/MoO₃ (red). (b) Summary of reported PCE values for OPVs based on normal and inverted architectures featuring different HELs. (c) EQE spectra of OPVs featuring different HEL. The Δ EQE represents the difference between the two EQE spectra (i.e. EQE_{Br-2PACz/MoO3}-EQE_{MoO3}). (d) Photo-CELIV, (e) TPV spectra, and (f) light intensity dependence of $V_{\rm OC}$ for OPVs based on MoO₃ and Br-2PACz/MoO₃ HELs.

We fabricated OPVs with an inverted cell architecture to study the effect of the different HELs (Fig. 1a). Fig. 2a shows representative J-V curves for OPVs with MoO₃ and Br-2PACz/MoO₃, while **Table 1** summarises the cell parameters. In devices featuring the MoO₃ HEL, a PCE of 17.36% is achieved, along with an open-circuit voltage ($V_{\rm OC}$) of 0.848 V, a short-circuit current (J_{SC}) of 26.17 mA/cm², a fill factor (FF) of 78.2%, and series resistance (R_s) of 1.95 Ω cm². Remarkably, OPVs based on the hybrid Br-2PACz/MoO₃ HEL show a maximum PCE of 18.73% (uncertified), thanks to the larger $V_{\rm OC}(0.863 \text{ V})$, higher $J_{\rm SC}(27.05 \text{ mA/cm}^2)$, improved FF (80.3%), and lower Rs (1.57 Ω cm²). Moreover, the statistical variation of PCE measured from 20 Br-2PACz/MoO₃ cells (inset in Fig. 2a, Fig. S9, and Table S5) is somewhat smaller, indicating these devices can be fabricated with better reproducibility than MoO₃-only devices. To the best of our knowledge, this is the first study of a Br-2PACz-modified HEL in an inverted organic solar cell architecture, while the PCE of 18.73% is the highest value reported to date for inverted OPVs (Fig. **2b**). $^{1, 16, 24-32}$ The enhanced V_{OC} of devices utilizing hybrid Br-2PACz/MoO₃ HEL as compared to MoO₃ HEL (0.863 V vs. 0.848 V) is majorly because of the increased WF of anode obtained via UPS and Kelvin Probe (5.58 eV vs. 5.32 eV), which in agreement to the previous reports. 54-56

Table 1. Summary of the operating parameters of OPVs based on PM6:PM7-Si:BTP-eC9 BHJs measured under constant illumination of AM 1.5G (100 mW/cm²).

HEL	V _{oc} [V]	$J_{\rm SC}$ [mA/cm ²]	$J_{ m cal}$ [mA/cm ²]	FF [%]	PCE [%]	Rs [Ω cm ²]
	0.848	26.17	25.38	78.2	$17.36 (17.15 \pm 0.17)$	1.95
Br-2PACz/MoO ₃	0.863	27.05	26.22	80.3	$18.73 \ (18.42 \pm 0.15)$	1.57

^aThe PCE_{avg} values in brackets represent averages from 20 cells.

The higher J_{SC} measured for the Br-2PACz/MoO₃-based cells is due to their higher external quantum efficiency (EQE) (**Fig. 2c**). To this end, the integrated photocurrent density (J_{cal}) deduced directly from the EQE matches the J_{SC} within $\pm 3\%$ (**Table 1**). Compared to MoO₃-based OPVs, cells utilizing Br-2PACz/MoO₃ HELs exhibit higher EQE across the entire range from 400 to 900 nm. This enhancement becomes more apparent in the difference between the EQE spectra of the two devices (Δ EQE) plotted in **Fig. 2c**. The higher J_{SC} measured in Br-2PACz/MoO₃-based OPVs appears to originate from the increased absorption coefficient (**Fig. S10a**), which is in turn attributed to the redistribution of the donor and acceptor components within the BHJ in agreement with previous studies. ^{51,57}

To study the impact of the different HELs on the electronic processes within the resulting cells, we fabricated hole-only devices in conjunction with the space-charge limited current (SCLC) technique to obtain the hole mobility (μ_h) (**Fig. S10b & Table S6**).⁵⁸ We find the μ_h to increase from 3.31×10^{-4} for MoO₃-based devices to 4.37×10^{-4} cm² V⁻¹s⁻¹ for Br-2PACz/MoO₃-based ones. The increased mobility was corroborated by photo-induced charge-carrier extraction in linearly increasing voltage (photo-CELIV) measurements (**Fig. 2d**).⁵⁹ The carrier mobility (μ) in devices featuring Br-2APCz/MoO₃ is higher (3.4×10^{-4} cm² V⁻¹s⁻¹) than that in devices with MoO₃ (2.4×10^{-4} cm² V⁻¹s⁻¹). Transient photovoltage (TPV) measurements (**Fig. 2e**) reveal that devices based on

a Br-2APCz/MoO₃ exhibit a longer charge-carrier lifetime, τ , (11.5 µs) compared to cells with MoO₃ (10.1 µs), suggesting reduced carrier recombination. Additional insights into the recombination processes are gained by fitting the dependence of $V_{\rm OC}$ on the incident light intensity ($P_{\rm light}$) using the power law: $V_{\rm OC} \propto nkT/q \ln(P_{\rm light})$, where n is the slope, k is the Boltzmann constant, T is the temperature, and q is the elementary charge. A $V_{\rm OC}$ dependence on $P_{\rm light}$ larger than kT/q (n>1) would indicate monomolecular recombination attributed to the presence of traps. As depicted in Fig. 2f, OPVs featuring Br-2APCz/MoO₃ yield 1.05 kT/q, which is lower than that for cells with MoO₃ (1.18 kT/q), suggesting reduced trap-assisted carrier recombination. These data further highlight the multiple benefits that Br-2APCz/MoO₃ has on device operation.

To demonstrate the applicability of this Br-2PACz/MoO₃ hybrid HEL approach, the BHJ systems based on PM6:IT-4F and PM6:IT-2Cl are investigated as shown in **Fig. S11** and **Table S7**. The OPV devices based on PM6:IT-4F with hybrid HEL exhibited an increased PCE as compared to MoO₃ one (13.25% *vs*.12.43%), while the PM6:IT-4F BHJ based on cells utilizing Br-2PACz/MoO₃ had an enhanced PCE than the devices with MoO₃ one (13.29% *vs*. 12.81%), demonstrating that the Br-2PACz/MoO₃ hybrid HEL is also potentially applicable to other BHJ systems.

To assess the impact of Br-2PACz/MoO₃ on the stability of the ensuing OPVs, we performed T₈₀ lifetime measurements, where T₈₀ is defined as the time taken for the cell's PCE to drop to 80% of its initial value under continuous solar illumination at 100 mW cm⁻² (**Fig. 3a**) and thermal heating at 80 °C (**Fig. 3b**) in an inert atmosphere. The stability of inverted MoO₃ and Br-2PACz/MoO₃-based OPVs were compared against cells made of the same BHJ system but featuring PEDOT:PSS and Br-2PACz as the HEL in standard cell architecture (optimized cell). From the continuous illumination results presented in **Fig. 3a**, it is evident that the OPV with

PEDOT:PSS exhibits the shortest T₈₀ (less stable) of 28 h, followed by the Br-2PACz-based cells with a T₈₀ = 101 h, which is comparable to our previous result.⁴² Although the Br-2PACz HEL enhances the stability of OPVs with standard architecture, its T₈₀ value remains significantly lower than that of cells with inverted architecture (101 h vs. 297 h). This finding highlights the advantage of the inverted device architecture in agreement with previous reports.^{6, 23}Remarkably, inverted OPVs featuring Br-2PACz/MoO₃ show yet more stable behaviour with a significantly longer T₈₀ of 615 h. Furthermore, the data shows that the presence of Br-2PACz plays a vital role in the cell's reliability, which is likely related to the differences in the microstructure of the BHJ discussed earlier. Monitoring the degradation of the PCE while maintaining the devices at 80 °C (**Fig. 3b**) provides complementary data on the degradation behaviours. Evidently, PEDOT:PSS and Br-2PACz-based OPVs with standard architecture exhibit the shorter T₈₀ of 93 h and 152 h, as compared to 731 h and 1061 h measured for cells based on MoO₃ and Br-2PACz/MoO₃ HELs, respectively. The remarkably higher stability of the Br-2PACz/MoO₃-based OPVs demonstrates the unique ability of this hybrid HEL to boost both the PCE and the operational stability of OPVs.

To elucidate the factors underpinning the improved cell stability, we performed ToF-SIMS measurements on both MoO₃ and Br-2PACz/MoO₃-based OPVs before (fresh) and after ageing (aged). The ageing step was implemented by subjecting the two types of cells to continuous illumination (100 mW cm⁻²) for 300 h, followed by non-stop heating at 80 °C for 500 h, after which ToF-SIMS measurements were performed. As shown in **Fig. 3c**, freshly prepared MoO₃-based cells exhibit a strong initial Mo⁻ signal (top surface of the sample) followed by the CN-signal, which is associated with the C9 acceptor. Although the aged MoO₃-based cell shows similar features, the decrease in the Mo⁻ signal as a function of sputtering time (i.e. sample depth) is more gradual (smaller slope). Fitting the degradation rates for the two samples yields slopes of -0.082

and -0.039 for the fresh and aged cells, respectively. The higher slope for the fresh sample indicates the presence of a sharper BHJ/MoO₃ interface, while the smaller slope for the aged sample is attributed to the diffusion of Mo ions into the BHJ upon ageing. In addition, the full width at half maximum (FWHM) is obtained by fitting Mo⁻ signal. Both of the aged devices exhibit increased FWHM, suggesting that Mo diffused into BHJ after aging test. However, the Br-2PACz/MoO₃-based achieve lower FHWM as compared to MoO₃-based one (17.4 vs. 28.4), suggesting that the diffused depth of Mo in BHJ is shallower than that in the pristine MoO₃-based device. Our finding agrees with previous studies that showed thermal annealing promotes the diffusion of MoO₃-related species away from the BHJ/MoO₃ interface and deeper into the BHJ, resulting in performance degradation.^{44, 61}Thus, introducing the Br-2PACz between the BHJ and MoO₃ partially suppresses the diffusion of Mo into the BHJ during ageing (**Fig. 3d**), as indicated by the relatively similar decay slope for aged (-0.051) and fresh samples (-0.085).

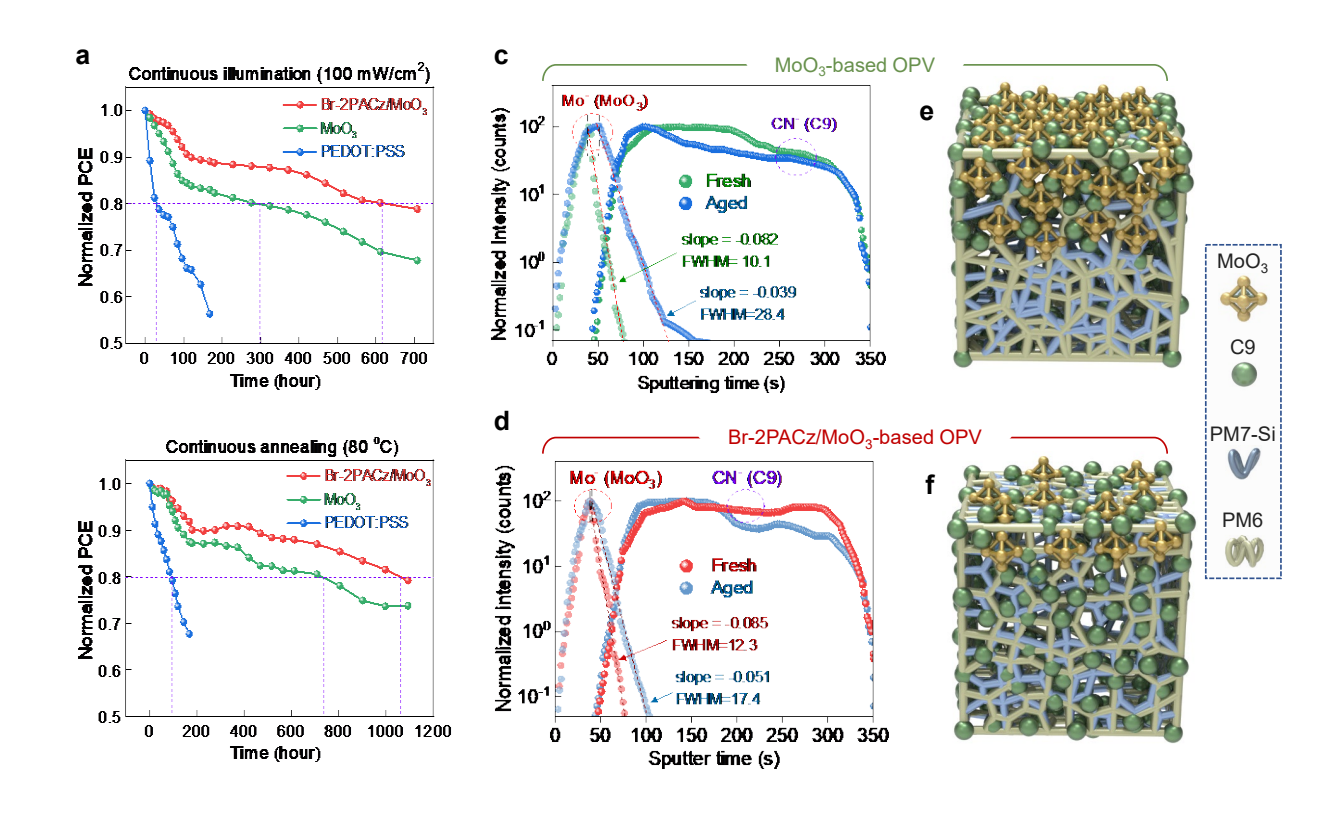


Fig. 3. Evolution of normalized PCEs of PM6:PM7-Si:BTP-eC9 OPVs based on MoO₃, Br-2APCz/MoO₃, Br-2PACz, and PEDOT:PSS as the HEL. The cell structure featuring Br-2PACz and PEDOT:PSS as the HEL are ITO/HEL/BHJ/PFN-Br/Ag. (a) PCE versus continuous illumination time (AM 1.5 G, 100 mW cm⁻²) in a nitrogen atmosphere. (b) PCE versus continuous heating time of the cell at 80 °C in a nitrogen atmosphere. ToF-SIMS signal intensity versus sputtering time (depth) of fresh and aged devices based on; (c) MoO₃, and (d) Br-2PACz/MoO₃ HELs. (e-f) Schematics depicting the distribution of MoO₃ and the various organic semiconductors across the BHJ for MoO₃ and Br-2PACz/MoO₃-based cells, respectively.

Apart from the Mo diffusion, the vertical phase separation of the donors and acceptor materials in the BHJ upon ageing also plays an important role. Thus, understanding this critical process is of considerable scientific and commercial interest. From the ToF-SIMS data in Fig. 3c and the complementary analysis of the donor polymers (PM6, PM7-Si) presented in Fig. S12, the ageing step of MoO₃-based cells leads to pronounced segregation of BTP-eC9 component closer to the top BHJ/HEL interface. On the other hand, PM6 segregates closer to the bottom ETL/BHJ interface (Fig. S12a), while the distribution of PM7-Si remains unaltered (Fig. S12b). OPVs based on Br-2PACz/MoO₃ exhibit different trends and degrees of component separation upon ageing. Specifically, PM6 appears to retain its concentration profile across the BHJ after ageing (Fig. S12c), whilst PM7-Si appears to segregate closer to the bottom BHJ/ETL interface (Fig. S12d). We attribute this to the different surface energies of the HEL and ETL systems (59.7 vs. 42.8 mN/m) and the tendency for the BHJ to minimize its free energy during the ageing steps.

For ease of comparison, the signals of CN⁻ (C9 acceptor), F⁻ (PM6 donor), and Si⁻ (PM7 donor) for the aged cells with MoO₃ and Br-2PACz/MoO₃ as HELs are all plotted in **Fig. S13**. Interestingly, both cells exhibit a relatively unfavourable component distribution since a large concentration of C9 is present closer to the hole-extracting BHJ/HEL interface. Interestingly, in Br-2PACz/MoO₃-based cells, the donors and the acceptor components appear to be more uniformly distributed across the BHJ, signifying an improved morphology. This is possibly due to

the small surface energy difference between the Br-2PACz/MoO₃ and the ETL (43.7 *vs.* 42.8 mN/m), ultimately improving the material distribution and cell performance (PCE and T₈₀).⁵⁰ Furthermore, we tracked the WF of Ag/MoO₃ and Ag/MoO₃/Br-2PACz anodes, obtained via Kelvin Probe, continuously illuminated at 100 mW/cm². As presented in **Fig. S14**, the WF of Ag/MoO₃ drop greatly during the aging test, which is in agreement with the previous report.^{62, 63} Moreover, the WF of Ag/MoO₃/Br-2PACz is more stable than the Ag/MoO₃, resulting in more stable performance when applied in the devices. **Fig. 3e-f** show schematics depicting the effect of the MoO₃ and Br-2PACz/MoO₃ HELs on the distribution of the material across the BHJ layer. The primary conclusion we can draw from these results is that Br-2PACz has two primary functions during cell ageing. Firstly, it partially blocks the diffusion of Mo-based ions into BHJ, and secondly, it improves the distribution of the two donor polymers and NFA across the BHJ. Lastly, the addition of Br-2PACz could increase the stability of WF of the anode during aging test.

The significant differences in the distribution of materials across the BHJ and the critical interfaces also affect the electrical properties of the OPVs. **Fig. S15** shows the Nyquist plots from where the interface and the BHJ resistances are calculated and summarized in **Table S8**. Due to material redistribution, cells featuring MoO₃ HEL exhibit an increased interface resistance (R_{inter}) from 50.3 Ω (fresh) to 103.4 Ω upon aging. The resistance associated with the BHJ (R_{bhj}) also undergoes a significant increase from 152.5 Ω , for the fresh cell, to 280.4 Ω upon aging due to changes in its internal microstructure, i.e. segregation of the donors and acceptor components. In addition, the presence of Br-2PACz suppresses these adverse effects, with the induced changes in R_{bhj} (173.8 Ω vs. 120.8 Ω) and R_{inter} (55.6 Ω vs. 36.7 Ω) remaining moderate as compared to fresh Br-2PACz/MoO₃ one.

Finally, the atomic-scale mechanisms of Br-2PACz interaction with MoO₃ and its effect on the WF of the latter were probed with Density Functional Theory (DFT) calculations (see *Supporting Information*). Since molybdenum oxide is often grown as substoichiometric with respect to its O content, we employed a three-layer MoO_{2.75} slab with O vacancies uniformly distributed in all layers (**Fig. S16**). For this structure, we found a WF of 6.33 eV, a value which is in the range of experimentally measured WFs for MoO_x (**Fig. S16a**),⁶⁴ but much larger than the above-mentioned measured WF value of 5.32 eV. We thus considered the effect water molecules might have when adsorbed on MoO_x, as highlighted in previous experimental works.⁶⁴ We find that water molecules can readily chemisorb (with an energy gain of >0.6 eV) as intact H₂O groups on the O vacancies of these surfaces by forming Mo-O bonds to under-coordinated surface Mo atoms. In this manner, the absolute value of the work function drops significantly and ranges between 5.27-5.64 eV (**Fig. S16b**). In particular, the high value (5.64 eV) is obtained for the H₂O-covered termination with H bonds between the H₂O groups and neighbouring O surface atoms, whereas in the case of the low WF value (5.27 eV), such H bonds are missing (**Fig. S16c-d**).

As shown in **Fig. S17**, Br-2PACz molecules can also readily form bonds (with an energy gain of about 1.55 eV per molecule) through the O atoms of their phosphonic acid groups with under-coordinated surface Mo atoms. Moreover, they can react similarly with H₂O-covered MoO_x surfaces to replace the chemisorbed H₂O groups, as depicted in **Fig. S18**. Notably, the reaction of Br-2PACz with MoO_x (**Fig. S18a**) changes the WF of the top (bottom) surface of the MoO_{2.75} slab to 5.29 eV (5.60 eV). If the physisorbed H₂O species are removed from this structure, the WF of the top (bottom) surface becomes 5.25 eV (5.51 eV) as shown in **Fig. S18b**. It should be noted that the different WF values for the two surfaces (top and bottom) stem from the fact that, despite both being coated with Br-2PACz molecules, they differ in terms of their H bond among their surface

O atoms. The DFT results confirm that Br-2PACz molecules can react with the MoO_x layers and form stable Mo-O bonds. In terms of the work functions, the calculated WFs for the Br-2PACz/MoO_x case are in satisfactory agreement with the experimental value of 5.6 eV, especially if one considers that the Br-2PACz configurations and level of coverage are expected to vary in actual samples. However, the detailed study of such variations goes beyond the scope of the atomistic DFT study presented here.

In summary, we developed a simple-to-implement hybrid HEL system that enhances the power conversion efficiency and stability of inverted OPVs. Incorporating the Br-2PACz molecule between the BHJ and MoO₃ increased the PCE of the cells from 17.36% to 18.73% (uncertified). The major improvement was attributed to multiple synergistic effects, including the formation of favourable hole-extracting interface energetics, advantageous vertical segregation of the donors and acceptor components within the BHJ, improved hole extraction, higher charge-carrier mobilities, longer carrier lifetimes, and suppressed carrier recombination. Notably, the T₈₀ of the inverted Br-2PACz/MoO₃-based OPVs increased to 615 and 1064 h under continuous solar illumination (1 sun) and heating (80 °C), respectively, compared to 297 and 731 h for MoO₃-based OPVs. The stability improvement was attributed, firstly, to the ability of the Br-2PACz layer to partially suppress the diffusion of Mo ions into the BHJ and, secondly, its beneficial effect on driving the phase separation of the donor and acceptor components close to the BHJ/HEL interface. The present work represents a step toward advancing the performance and commercialization prospects of OPVs.

Author contributions

Y.L. and T.D.A conceived the idea. Y.L. fabricated, optimized, characterized the photovoltaic devices. Y.Z., A. M, J. Z., S.B., and S.R.M. synthesized the self-assembled monolayer materials. E.G. and V.G. contributed to the DFT calculations. X.Z and A.E contributed to morphology characterization. All authors contributed to editing the manuscript. T.D.A supervised and directed the project.

Conflict of Interest

The authors declare no conflict of interest.

ACKNOWLEDGMENT

This publication is based upon work supported by the King Abdullah University of Science and Technology (KAUST) Office of Sponsored Research (OSR) under Awards No: OSR-2018-CARF/CCF-3079 and No: OSR-2019-CRG8-4095.3. Y. Z., J. Z., S. B., and S. R. M. acknowledge funding from NSF under the CCI Center for Selective C–H Functionalization (CHE-1700982) and from the Department of the Navy, Office of Naval Research as part of a Multidisciplinary University Research Initiative, Award No., N00014-21-1-2180. E. G. and L. T. acknowledge support for the computational time granted from GRNET in the National HPC facility -ARIS - under project ATOMA. A.M. and V.G. acknowledge funding from the Research Council of Lithuania under grant agreement Nr. 01.2.2-LMT-K-718-03-0040 (SMARTMOLECULES).

REFERENCES

- 1. Y. Y. Jiang, X. Y. Dong, L. L. Sun, T. F. Liu, F. Qin, C. Xie, P. Jiang, L. Hu, X. Lu, X. M. Zhou, W. Meng, N. Li, C. J. Brabec and Y. H. Zhou, *Nat. Energy* 2022, **7**, 352-359.
- 2. Y. Lin, B. Adilbekova, Y. Firdaus, E. Yengel, H. Faber, M. Sajjad, X. Zheng, E. Yarali, A. Seitkhan and O. M. Bakr, *Adv. Mater.*, 2019, **31**, 1902965.
- 3. Y. Li, X. Huang, K. Ding, H. K. M. Sheriff, Jr., L. Ye, H. Liu, C. Z. Li, H. Ade and S. R. Forrest, *Nat. Commun.*, 2021, **12**, 5419.
- 4. Y. Zhang, C. Duan and L. Ding, Sci. Bull., 2020, 65, 2040-2042.
- 5. M. Yang, W. Wei, X. Zhou, Z. Wang and C. Duan, *Energ. Mater.*, 2021, 1, 100008.
- 6. G. Zhang, F. R. Lin, F. Qi, T. Heumuller, A. Distler, H. J. Egelhaaf, N. Li, P. C. Y. Chow, C. J. Brabec, A. K. Jen and H. L. Yip, *Chem. Rev.*, 2022, **122**, 14180-14274.
- 7. S. X. Li, C. Z. Li, M. M. Shi and H. Z. Chen, *ACS Energy Lett.*, 2020, **5**, 1554-1567.
- 8. H. Yao and J. Hou, *Angew. Chem. Int. Edit.*, 2022, **61**, 202209021.
- 9. B. Wu, B. Yin, C. Duan and L. Ding, J. Semicond., 2021, 42, 080301.
- 10. L. Zhu, M. Zhang, J. Xu, C. Li, J. Yan, G. Zhou, W. Zhong, T. Hao, J. Song, X. Xue, Z. Zhou, R. Zeng, H. Zhu, C. C. Chen, R. C. I. MacKenzie, Y. Zou, J. Nelson, Y. Zhang, Y. Sun and F. Liu, *Nat. Mater.*, 2022, **21**, 656-663.
- 11. P. Bi, S. Zhang, Z. Chen, Y. Xu, Y. Cui, T. Zhang, J. Ren, J. Qin, L. Hong, X. Hao and J. Hou, *Joule*, 2021, **5**, 2408-2419.
- 12. Y. Cui, Y. Xu, H. Yao, P. Bi, L. Hong, J. Zhang, Y. Zu, T. Zhang, J. Qin, J. Ren, Z. Chen, C. He, X. Hao, Z. Wei and J. Hou, *Adv. Mater.*, 2021, **33**, 2102420.
- 13. Y. Lin, H. Chen, S. Y. Jeong, J. Tian, D. R. Naphade, Y. Zhang, M. Alsufyani, W. Zhang, S. Griggs, H. Hu, S. Barlow, H. Y. Woo, S. R. Marder, T. D. Anthopoulos and I. McCulloch, *Energ. Environ. Sci.*, 2023, DOI: 10.1039/d2ee03483b.
- 14. Y. Firdaus, V. M. Le Corre, J. I. Khan, Z. Kan, F. Laquai, P. M. Beaujuge and T. D. Anthopoulos, *Adv. Sci.*, 2019, **6**, 1802028.
- 15. Y. Lin, M. I. Nugraha, Y. Firdaus, A. D. Scaccabarozzi, F. Aniés, A.-H. Emwas, E. Yengel, X. Zheng, J. Liu, W. Wahyudi, E. Yarali, H. Faber, O. M. Bakr, L. Tsetseris, M. Heeney and T. D. Anthopoulos, *ACS Energy Lett.* 2020, **5**, 3663-3671.
- 16. Y. B. Lin, Y. Firdaus, M. I. Nugraha, F. Liu, S. Karuthedath, A. H. Emwas, W. M. Zhang, A. Seitkhan, M. Neophytou, H. Faber, E. Yengel, I. McCulloch, L. Tsetseris, F. Laquai and T. D. Anthopoulos, *Adv. Sci.*, 2020, 7.
- 17. W. Peng, Y. Lin, S. Y. Jeong, Z. Genene, A. Magomedov, H. Y. Woo, C. Chen, W. Wahyudi, Q. Tao, J. Deng, Y. Han, V. Getautis, W. Zhu, T. D. Anthopoulos and E. Wang, *Nano Energy*, 2022, **92**, 106681.
- 18. R. Sun, Y. Wu, X. Yang, Y. Gao, Z. Chen, K. Li, J. Qiao, T. Wang, J. Guo, C. Liu, X. Hao, H. Zhu and J. Min, *Adv. Mater.*, 2022, **34**, 2110147.
- 19. K. Chong, X. Xu, H. Meng, J. Xue, L. Yu, W. Ma and Q. Peng, *Adv. Mater.*, 2022, **34**, e2109516.
- 20. V. Shrotriya, G. Li, Y. Yao, C. W. Chu and Y. Yang, *Appl. Phys. Lett.*, 2006, **88**, 073508.
- 21. A. K. K. Kyaw, X. W. Sun, C. Y. Jiang, G. Q. Lo, D. W. Zhao and D. L. Kwong, *Appl. Phys. Lett.*, 2008, **93**, 221107.
- 22. K. A. Mazzio and C. K. Luscombe, Chem. Soc. Rev., 2015, 44, 78-90.
- 23. X. Xu, J. Xiao, G. Zhang, L. Wei, X. Jiao, H.-L. Yip and Y. Cao, *Sci. Bull.*, 2020, **65**, 208-216.
- 24. C. Li, J. Zhou, J. Song, J. Xu, H. Zhang, X. Zhang, J. Guo, L. Zhu, D. Wei and G. Han, *Nat. Energy*, 2021, **6**, 605-613.

- 25. J. Huang, D. Zhao, Z. F. Dou, Q. S. Fan, N. Li, S. H. Peng, H. R. Liu, Y. D. Jiang, J. S. Yu and C. Z. Li, *Energ. Environ. Sci.*, 2021, **14**, 3010-3018.
- 26. Z. Abbas, S. U. Ryu, M. Haris, C. E. Song, H. K. Lee, S. K. Lee, W. S. Shin, T. Park and J. C. Lee, *Nano Energy*, 2022, **101**, 107574.
- 27. X. Song, G. Liu, W. Gao, Y. Di, Y. Yang, F. Li, S. Zhou and J. Zhang, *Small*, 2021, **17**, 2006387.
- 28. C. Zhu, J. Yuan, F. Cai, L. Meng, H. Zhang, H. Chen, J. Li, B. Qiu, H. Peng, S. Chen, Y. Hu, C. Yang, F. Gao, Y. Zou and Y. Li, *Energ. Environ. Sci.*, 2020, **13**, 2459-2466.
- 29. Y. Cui, H. Yao, J. Zhang, T. Zhang, Y. Wang, L. Hong, K. Xian, B. Xu, S. Zhang, J. Peng, Z. Wei, F. Gao and J. Hou, *Nat. Commun.*, 2019, **10**, 2515.
- 30. C. Sun, S. Qin, R. Wang, S. Chen, F. Pan, B. Qiu, Z. Shang, L. Meng, C. Zhang, M. Xiao, C. Yang and Y. Li, *J. Am. Chem. Soc.*, 2020, **142**, 1465-1474.
- 31. H. Wang, T. Liu, J. Zhou, D. Mo, L. Han, H. Lai, H. Chen, N. Zheng, Y. Zhu, Z. Xie and F. He, *Adv. Sci.*, 2020, **7**, 1903784.
- 32. Y. Yang, J. W. Wang, P. Q. Bi, Q. Kang, Z. Zheng, B. W. Xu and J. H. Hou, *Chem. Mater.*, 2022, **34**, 6312-6322.
- 33. Y. Wei, Z. Chen, G. Lu, N. Yu, C. Li, J. Gao, X. Gu, X. Hao, G. Lu, Z. Tang, J. Zhang, Z. Wei, X. Zhang and H. Huang, *Adv. Mater.*, 2022, **34**, 2204718.
- 34. W. Gao, F. Qi, Z. Peng, F. R. Lin, K. Jiang, C. Zhong, W. Kaminsky, Z. Guan, C. S. Lee, T. J. Marks, H. Ade and A. K. Jen, *Adv. Mater.*, 2022, **34**, 2202089.
- 35. L. Zhan, S. Li, Y. Li, R. Sun, J. Min, Z. Bi, W. Ma, Z. Chen, G. Zhou, H. Zhu, M. Shi, L. Zuo and H. Chen, *Joule*, 2022, **6**, 662-675.
- 36. Y. Cai, Y. Li, R. Wang, H. Wu, Z. Chen, J. Zhang, Z. Ma, X. Hao, Y. Zhao, C. Zhang, F. Huang and Y. Sun, *Adv. Mater.*, 2021, **33**, 2101733.
- 37. T. Zhang, C. An, P. Bi, Q. Lv, J. Qin, L. Hong, Y. Cui, S. Zhang and J. Hou, *Adv. Energy Mater.*, 2021, **11**, 2101705.
- 38. Y. Lin, A. Magomedov, Y. Firdaus, D. Kaltsas, A. El-Labban, H. Faber, D. R. Naphade, E. Yengel, X. Zheng, E. Yarali, N. Chaturvedi, K. Loganathan, D. Gkeka, S. H. AlShammari, O. M. Bakr, F. Laquai, L. Tsetseris, V. Getautis and T. D. Anthopoulos, *ChemSusChem*, 2021, 14, 3569-3578.
- 39. J. Jing, S. Dong, K. Zhang, B. Xie, J. Zhang, Y. Song and F. Huang, *Nano Energy*, 2022, **93**, 106814.
- 40. Y. Lin, Y. Firdaus, F. H. Isikgor, M. I. Nugraha, E. Yengel, G. T. Harrison, R. Hallani, A. El-Labban, H. Faber, C. Ma, X. Zheng, A. Subbiah, C. T. Howells, O. M. Bakr, I. McCulloch, S. D. Wolf, L. Tsetseris and T. D. Anthopoulos, *ACS Energy Letters*, 2020, 5, 2935-2944.
- 41. J. Jing, S. Dong, K. Zhang, Z. Zhou, Q. Xue, Y. Song, Z. Du, M. Ren and F. Huang, *Adv. Energy Mater.*, 2022, **12**, 2200453.
- 42. Y. Lin, Y. Zhang, J. Zhang, M. Marcinskas, T. Malinauskas, A. Magomedov, M. I. Nugraha, D. Kaltsas, D. R. Naphade, G. T. Harrison, A. El Labban, S. Barlow, S. De Wolf, E. Wang, I. McCulloch, L. Tsetseris, V. Getautis, S. R. Marder and T. D. Anthopoulos, *Adv. Energy Mater.*, 2022, 12, 2202503.
- 43. L. Guo, Q. Li, J. Ren, Y. Xu, J. Zhang, K. Zhang, Y. Cai, S. Liu and F. Huang, *Energ. Environ. Sci*, 2022, **15**, 5137-5148.
- 44. Y. Yin, X. Pan, M. R. Andersson, D. A. Lewis and G. G. Andersson, *ACS Appl. Energ. Mater.*, 2019, **3**, 366-376.

- 45. T. Yang, M. Wang, C. Duan, X. Hu, L. Huang, J. Peng, F. Huang and X. Gong, *Energ. Environ. Sci.*, 2012, **5**, 8208.
- W. Peng, Y. Lin, S. Y. Jeong, Y. Firdaus, Z. Genene, A. Nikitaras, L. Tsetseris, H. Y. Woo, W. Zhu, T. D. Anthopoulos and E. Wang, *Chem. Mater.*, 2021, **33**, 7254-7262.
- 47. Z. F. Ma, Z. Tang, E. G. Wang, M. R. Andersson, O. Inganas and F. L. Zhang, *J. Phys. Chem. C*, 2012, **116**, 24462-24468.
- 48. Y. Lin, Y. Jin, S. Dong, W. Zheng, J. Yang, A. Liu, F. Liu, Y. Jiang, T. P. Russell and F. Zhang, *Adv. Energy Mater.*, 2018, **8**, 1701942.
- 49. M. Campoy-Quiles, T. Ferenczi, T. Agostinelli, P. G. Etchegoin, Y. Kim, T. D. Anthopoulos, P. N. Stavrinou, D. D. Bradley and J. Nelson, *Nat Mater*, 2008, 7, 158-164.
- 50. Y. P. Qin, N. Balar, Z. X. Peng, A. Gadisa, I. Angunawela, A. Bagui, S. Kashani, J. H. Hou and H. Ade, *Joule*, 2021, **5**, 2129-2147.
- 51. L. Huang, G. Wang, W. Zhou, B. Fu, X. Cheng, L. Zhang, Z. Yuan, S. Xiong, L. Zhang, Y. Xie, A. Zhang, Y. Zhang, W. Ma, W. Li, Y. Zhou, E. Reichmanis and Y. Chen, *ACS Nano*, 2018, **12**, 4440-4452.
- 52. J. K. Tan, R. Q. Png, C. Zhao and P. K. H. Ho, Nat. Commun., 2018, 9, 3269.
- 53. S. Braun, W. R. Salaneck and M. Fahlman, *Adv. Mater.*, 2009, **21**, 1450-1472.
- 54. R. Steim, F. R. Kogler and C. J. Brabec, *J. Mater. Chem.*, 2010, **20**, 2499-2512.
- 55. E. L. Ratcliff, A. Garcia, S. A. Paniagua, S. R. Cowan, A. J. Giordano, D. S. Ginley, S. R. Marder, J. J. Berry and D. C. Olson, *Adv. Energy Mater.*, 2013, **3**, 647-656.
- 56. J. Cheng, F. Xie, Y. Liu, W. E. I. Sha, X. Li, Y. Yang and W. C. H. Choy, *J. Mater. Chem. A*, 2015, **3**, 23955-23963.
- 57. C. Duan, C. Zhong, F. Huang and Y. Cao, in *Organic Solar Cells: Materials and Device Physics*, ed. W. C. H. Choy, Springer London, London, 2013, DOI: 10.1007/978-1-4471-4823-4 3, pp. 43-79.
- 58. V. D. Mihailetchi, J. Wildeman and P. W. Blom, *Phys. Rev. Lett.*, 2005, **94**, 126602.
- 59. T. M. Clarke, C. Lungenschmied, J. Peet, N. Drolet and A. J. Mozer, *Adv. Energy Mater.*, 2015, **5**, 1401345.
- 60. A. K. Kyaw, D. H. Wang, V. Gupta, W. L. Leong, L. Ke, G. C. Bazan and A. J. Heeger, *ACS Nano*, 2013, **7**, 4569-4577.
- 61. Y. Gong, Y. Dong, B. Zhao, R. Yu, S. Hu and Z. a. Tan, *J. Mater. Chem. A*, 2020, **8**, 978-1009.
- 62. C. Yang, S. Zhan, Q. Li, Y. Wu, X. Jia, C. Li, K. Liu, S. Qu, Z. Wang and Z. Wang, *Nano Energy*, 2022, **98**, 107299.
- 63. W. Greenbank, N. Rolston, E. Destouesse, G. Wantz, L. Hirsch, R. Dauskardt and S. Chambon, *J. Mater. Chem. A*, 2017, **5**, 2911-2919.
- 64. I. Irfan, A. J. Turinske, Z. N. Bao and Y. L. Gao, *Appl. Phys. Lett.*, 2012, **101**, 093305.